Research Square

Preprints are preliminary reports that have not undergone peer review.
They should not be considered conclusive, used to inform clinical practice,
or referenced by the media as validated information.

Adipocyte-Derived β-Hydroxybutyrate Confers Metabolic Stress Resistance in Multiple Myeloma

Zongwei Li

lizongwei@ahmu.edu.cn

Anhui Medical University

Chen Song

Anhui Medical University

Peng Yang

Shanxi University

Yu Li

Anhui Medical University

Tao Xia

Anhui Medical University

Rui Li

Anhui Medical University

Wenjun Li

Anhui Medical University

Yansheng Wang

Second Affiliated Hospital of Anhui Medical University

Tiantian Jia

Anhui Medical University

Chenfeng Liu

Anhui Medical University

Xunxia Bao

Anhui Medical University

Qi Wang

Anhui Medical University

Yuan Yao

Anhui Medical University

Qian Dai

Anhui Medical University

Wei Wei

First Affiliated Hospital of Anhui Medical University

Huan Liu

Xiamen University

Junjie Lv

First Affiliated Hospital of Anhui Medical University

Article

Keywords: Multiple myeloma, adipocytes, β-hydroxybutyrate, IRF4, acetylation

Posted Date: June 19th, 2025

DOI: https://doi.org/10.21203/rs.3.rs-6598368/v1

License: This work is licensed under a Creative Commons Attribution 4.0 International License.
Read Full License

Additional Declarations: There is **NO** Competing Interest.

Version of Record: A version of this preprint was published at Nature Communications on August 11th, 2026. See the published version at https://doi.org/10.1038/s41467-026-76595-0.

Abstract

Despite being recognized as a major mesenchymal cell type and a key accomplice in myeloma progression, the precise roles of adipocytes in distinct stages of myeloma pathogenesis remain elusive. Here, we elucidate a critical role of adipocyte-derived β-hydroxybutyrate (β-OHB) in enabling myeloma cells to overcome glucose metabolic stress by sustaining the stability of interferon regulatory factor 4 (IRF4), a master oncoprotein essential for myeloma survival. Under glucose deprivation conditions, AMP-activated protein kinase (AMPK) activation disrupts the IRF4-heat shock protein 90 (HSP90) interaction, enabling the E3 ligase TRIM21-mediated IRF4 ubiquitination and proteasomal degradation. Adipocytes-secreted β-OHB counteracts this process by fueling 3-oxoacid CoA-transferase 1 (OXCT1)-dependent ketolysis and activating N-acetyltransferase 10 (NAT10) to acetylate IRF4 at lysine 87, thereby restoring IRF4-HSP90 binding and blocking TRIM21-mediated IRF4 degradation. Notably, pharmacological inhibition of OXCT1 or NAT10, combined with AMPK activator, synergistically suppresses myeloma growth *in vitro* and *in vivo*. Our study thus positions adipocytes-derived β-OHB as a critical metabolic adaptor that empowers myeloma cells to circumvent glucose metabolic stress and highlights a promising therapeutic avenue for targeting metabolic vulnerabilities in multiple myeloma.

INTRODUCTION

Multiple myeloma (MM) is an incurable hematologic malignancy characterized by the clonal proliferation of plasma cells, representing the second most common hematologic cancer after chronic lymphocytic leukemia [1, 2]. Despite advancements in therapeutic strategies, the median survival for myeloma patients has stagnated at 5 to 7 years, and a complete cure remains a formidable challenge. MM is typically a disease of middle-aged and older people. Epidemiological evidence also supports obesity as a strong risk factor for the pathogenesis of myeloma [3–5]. Notably, both aging and obesity, key risk factors for MM prevalence, are concomitant with impaired bone marrow osteogenic regeneration and adipose tissue expansion [6, 7], making adipocyte one of the most abundant cell types in bone marrow.

We previously demonstrated that myeloma cells epigenetically reprogram adipocytes, prompting them to secrete adipokines that activate osteoclastogenesis and suppress osteoblastogenesis, thereby contributing to myeloma-induced bone disease [8]. Moreover, we also revealed that, under obese conditions, adipocyte-derived angiotensin II (Ang II) impinges on acetyl-CoA synthetase 2 (ACSS2) and interferon regulatory factor 4 (IRF4) axis in myeloma cells, driving disease progression [9]. This discovery established adipocyte-ACSS2-IRF4 axis as an etiologically mechanistic link accounting for obesity-associated myeloma risk. Despite being recognized as a critical accomplice in multiple myeloma pathogenesis [10], the precise roles of adipocytes in distinct stages of myeloma pathogenesis and their implications for therapy remain incompletely understood.

Metabolic reprogramming is one of the hallmarks of cancer and has emerged as an attractive therapeutic target for cancer treatment [11]. A fundamental question in cancer metabolism is how cancer cells adapt to and survive metabolically adverse conditions such as nutrient deficiency, and whether

these adaptive mechanisms can be exploited as vulnerabilities for therapeutic intervention [12, 13]. Nutrient deficiency, caused by excessive tumor growth, low glycaemic diet, ketogenic diet or intermittent fasting, is often presumed to restrict tumor growth and survival by reducing glucose availability in the tumor microenvironment [14, 15]. As one of the major mesenchymal cell types in the myeloma microenvironment, whether and how adipocytes contribute to the resistance of myeloma cells to metabolic stresses are poorly understood.

To elucidate the role of adipocytes in myeloma pathogenesis under conditions of glucose metabolic stress, we utilized 2-deoxy-D-glucose (2-DG), a glucose analog that disrupts glycolytic metabolism, to model glucose deprivation (GD) *in vivo* [16, 17]. Our results reveal that adipocytes markedly enhance myeloma cell resistance to 2-DG-induced metabolic stress across different myeloma mouse models. Further investigation identified adipocyte-derived β-hydroxybutyric acid (β-OHB) as the key mediators of this adipocyte-driven protective effect. Mechanistically, myeloma cells harness β-OHB to activate the 3-oxoacid CoA-transferase 1 (OXCT1) and N-acetyltransferase 10 (NAT10) axis, which promotes IRF4 acetylation and prevents its TRIM21-mediated degradation under GD conditions. Importantly, we demonstrate that combining a metabolic stress inducer with a ketolysis inhibitor synergistically suppresses myeloma growth both *in vitro* and *in vivo*. This study unveils a previously unrecognized role of adipocyte-derived β-OHB in protecting against glucose metabolic stress and highlights a promising therapeutic avenue for targeting metabolic vulnerabilities in multiple myeloma and suggests viable therapeutic targets for multiple myeloma treatment.

RESULTS

Adipocytes confer myeloma cells resistance to 2-DG-induced metabolic stress in vivo

To explore the impact of adipocytes on myeloma progression under metabolic stress, we used a high-fat diet-induced obesity (DIO) model in C57BL/6J mice. The DIO mice were fed with a 60% kcal high-fat diet for 20 weeks to reach an obese state, while control mice received a standard 10% kcal normal diet (ND) (Figs. 1A and 1B). To establish myeloma, the murine Vk12598 myeloma cells were inoculated into the femurs of both DIO and ND mice. One week post-inoculation, 2-DG was administered to simulate GD conditions *in vivo*. Consistent with our previous findings [9], DIO mice exhibited significantly higher tumor burden compared to ND controls, as demonstrated by elevated serum M-protein levels (Fig. 1C), increased infiltration of $CD138^+$ myeloma cells in both bone marrow and spleen (Figs. 1D-1G), and pronounced splenomegaly (Fig. 1F). Strikingly, while 2-DG treatment markedly reduced tumor burden in ND mice, these effects were significantly attenuated in DIO mice (Figs. 1C-1G), suggesting that the obese state endows myeloma cells with the resistance to 2-DG-induced metabolic stress.

Excessive adipose tissue accumulation is one of the most prominent characteristics of obesity [18]. To investigate the role of adipocytes in conferring resistance to 2-DG-induced metabolic stress in myeloma cells, we subcutaneously co-implanted ARP1 myeloma cells with mature adipocytes into NCG mice. ARP1 cells implanted alone in the contralateral flank served as controls. Upon tumor palpation, mice

were administered 2-DG or vehicle control via intraperitoneal injection (Fig. 1H). Compared to vehicle-treated controls, 2-DG treatment significantly inhibited tumor growth in mice implanted with ARP1 cells alone, as demonstrated by reduced tumor growth rates, smaller tumor sizes, and lower tumor weights. However, these inhibitory effects of 2-DG were abrogated in the presence of co-injected adipocytes (Figs. 1H-1J). Immunohistochemical (IHC) analysis further revealed decreased Ki67 expression in 2-DG-treated tumors, an effect reversed by adipocyte co-implantation (Figs. 1K and 1L).

To further validate the role of adipocytes in promoting myeloma cell resistance to metabolic stress, luciferase-labeled ARP1 or 5TGM1 cells were co-injected with adipocytes into the femurs of NCG mice or TCRb^{tm1Mom}/J mice, respectively (Figures S1A and S1C). Compared to vehicle controls, 2-DG treatment significantly reduced bioluminescent activity at sites implanted with myeloma cells alone. In contrast, adipocyte co-implantation markedly enhanced myeloma cell resistance to 2-DG treatment (Figures S1A-S1D). Collectively, these findings indicate that adipocytes confer myeloma cells with the ability to resist 2-DG-induced metabolic stress *in vivo*.

Adipocyte-derived β-hydroxybutyrate confers resistance to glucose metabolic stress in myeloma cells in vitro and in vivo

To further explore the mechanism by which adipocytes promote myeloma cell resistance to glucose metabolic stress, ARP1 or 5TGM1 cells were cocultured with adipocytes under glucose deprivation (GD) conditions using a transwell system to mimic the *in vivo* microenvironment (Fig. 2A). In line with our *in vivo* findings, co-culture with adipocytes significantly improved the survival of both ARP1 and 5TGM1 cells under GD conditions (Fig. 2A). Furthermore, GD substantially reduced the protein levels of interferon regulatory factor 4 (IRF4), a decisive survival factor in myeloma [19]. Notably, this reduction in IRF4 expression was reversed by co-culture with adipocytes (Fig. 2B).

To pinpoint the effective factors from adipocytes, conditioned medium (AD-CM) was collected from adipocytes cultured under GD conditions. AD-CM was treated with proteinase K (ProK) or fractionated by molecular weight cutoff filtration and applied to ARP1 or 5TGM1 cells under GD conditions. AD-CM rescued GD-induced IRF4 reduction in myeloma cells, an effect that persisted after ProK treatment, thus ruling out proteins as the active components in AD-CM (Fig. 2C). Intriguingly, the < 3 kDa fraction of AD-CM, but not the > 3 kDa fraction, recapitulated the effects of unfractionated AD-CM, suggesting that small non-protein metabolites mediate the activity of AD-CM on IRF4 protein (Fig. 2C).

Metabolomic profiling of AD-CM under GD versus normal glucose conditions revealed 286 differentially regulated metabolites, comprising 167 downregulated and 119 upregulated metabolites (Fig. 2D). Figure 2E displays a heatmap of the most significantly altered metabolites. Notably, β-hydroxybutyrate (β-OHB), the predominant ketone body typically synthesized by the liver during metabolic stress [20, 21], was significantly elevated in AD-CM under GD conditions (Fig. 2F). Intriguingly, both β-OHB and acetoacetate (another unstable ketone body) effectively restored GD-induced IRF4 reduction in ARP1 and 5TGM1 cells (Fig. 2G). Moreover, β-OHB levels in patient bone marrow aspirates correlated strongly

with patients' BMI, implicating adipocytes may serve as an important extrahepatic source of ketone bodies (Fig. 2I).

To better understand the causal relationship between glucose deprivation and ketone body production in adipocytes, we analyzed the expression of ketogenic enzymes in adipocytes (Figure S2A). mRNA levels of *ACAT1*, *HMGCS2*, *HMGCL*, and *BDH1* were significantly upregulated under GD conditions (Figure S2B). To extend these findings *in vivo*, we examined the regulation of these enzymes in adipose tissues under metabolic stress. Consistent with previous studies demonstrating that caloric restriction induces browning of white adipose tissue (WAT) [22], alternate-day fasting (ADF) in C57BL/6J mice promoted a browning-like phenotype in both epididymal (eWAT) and inguinal (iWAT) white adipose tissue, as evidenced by increased UCP-1 expression (Figures S2C, S2E, S2G and S2H). In line with the our *in vitro* findings, ADF upregulated the expression of ketogenic enzymes in eWAT and iWAT (Figure S2D and S2F). Notably, Hmgcs2, the rate-limiting enzyme in ketogenesis, was elevated at the protein level in liver, eWAT, and iWAT following ADF (Figures S2I and S2J). These results suggest that glucose metabolic stress enhances the ketogenic enzyme expression in adipocytes.

To further assess the impact of adipocyte-derived β-OHB on the metabolic stress resistance of myeloma cells, we generated adipocyte-specific *Hmgcs2* knockout (*Hmgcs2*^{AKO}) mice by crossing *Hmgcs2*$^{flox/flox}$ mice with Adipoq-Cre transgenic mice (Figure S2K). *Hmgcs2* deletion in eWAT, iWAT, and brown adipose tissue (BAT) was confirmed by western blot analysis (Figure S2L). Subsequently, adipocytes isolated from both *Hmgcs2*^{WT} and *Hmgcs2*^{AKO} mice were co-cultured with myeloma cells under GD conditions. In concordance with our previous findings (Fig. 2A), wild-type adipocytes (AD^{WT}) significantly attenuated GD-induced IRF4 reduction in both ARP1 and 5TGM1 cells. However, this protective effect was substantially compromised in *Hmgcs2*-deficient adipocytes (AD^{KO}) (Fig. 2J). To validate these observations *in vivo*, we subcutaneously implanted 5TGM1 cells either alone or in combination with an equal number of AD^{WT} or AD^{KO} into nude mice. Following tumor establishment, mice were treated with 2-DG as previously described. Notably, co-implantation with AD^{WT} significantly rescued 2-DG-induced tumor growth suppression, whereas this protective effect was markedly attenuated in the AD^{KO} group, as demonstrated by tumor growth kinetics (Fig. 2K), final tumor sizes (Fig. 2L), and tumor weights (Fig. 2M). Collectively, these results demonstrate that glucose metabolic stress induces ketone body production in adipocytes, which in turn protects myeloma cells against metabolic stress (Figure S2M).

Glucose deprivation induces IRF4 degradation through disruption of IRF4-HSP90 interaction

To elucidate the mechanism whereby adipocyte-derived β-OHB protects myeloma cell survival under glucose metabolic stress, we first investigated how GD impaired IRF4 expression in myeloma cells. IRF4 mRNA and protein levels were assessed in human (ARP1, RPMI8226, ARH77) and murine (5TGM1) myeloma cells exposed to GD or 2-DG for varying durations. GD or 2-DG treatment significantly reduced IRF4 protein levels without affecting its mRNA levels across all tested cell lines (Figures S3A-S3D).

Furthermore, glucose deficiency decreased IRF4 protein but not mRNA levels in a concentration-dependent manner (Figures S3E and S3F). These findings suggest that GD and 2-DG regulate IRF4 expression through post-transcriptional mechanisms. Cycloheximide (CHX)-chase assays revealed accelerated IRF4 protein degradation in GD- or 2-DG-treated cells compared to controls (Figs. 3A-3D).

To determine the pathways mediating GD or 2-DG-induced IRF4 degradation, HA-IRF4-expressing myeloma cells were treated with inhibitors targeting distinct protein degradation pathways, including MG-132 and bortezomib (BTZ; proteasome inhibitors), leupeptin (a lysosomal protease inhibitor), and MDL-28170 (a calpain inhibitor), under GD conditions. Proteasome inhibitors MG-132 and BTZ, but not leupeptin or MDL-28170, effectively rescued GD-induced IRF4 degradation (Fig. 3E), indicating that GD destabilizes IRF4 via the ubiquitin-proteasome pathway. Consistent with this, GD treatment significantly enhanced K48-linked ubiquitination of IRF4 in ARP1 and RPMI8226 cells (Fig. 3F), a canonical signal for proteasomal degradation [23].

To further dissect the mechanism underlying GD-induced IRF4 degradation, we employed immunoprecipitation coupled with mass spectrometry (MS) to identify IRF4-interacting proteins under normal glucose and GD conditions. To assess this, ARP1 cells expressing HA-IRF4 were cultured in normal glucose or GD conditions. Anti-HA immunoprecipitation of cell lysates followed by mass spectrometry (MS) revealed decreased HSP90 binding to IRF4 under GD, alongside enhanced interactions with the E3 ubiquitin ligases TRIM21 and FBXW11 (Fig. 3G). To validate these findings, co-immunoprecipitation (Co-IP) assays were performed in HA-IRF4-expressing ARP1 cells exposed to GD or 2-DG. Under normal glucose conditions, HA-IRF4 formed a complex with endogenous HSP90; however, this interaction was abolished upon GD or 2-DG treatment (Fig. 3H). Similarly, in HEK293T cells co-transfected with Flag-HSP90 and HA-IRF4 plasmids, GD or 2-DG disrupted the interaction between Flag-HSP90 and HA-IRF4 (Figure S3G). Immunofluorescence staining further demonstrated that HSP90 co-localized with IRF4-GFP in the nucleus under normal glucose conditions, but GD induced nuclear export of HSP90 and disrupted its co-localization with IRF4-GFP (Fig. 3I).

To determine whether HSP90 plays a functional role in regulating IRF4 stability, we inhibited HSP90 using 17-AAG or depleted its expression via HSP90-specific shRNA in myeloma cells. Both approaches significantly reduced IRF4 protein levels across different myeloma cell lines (Figures S3H and S3I). CHX-chase assays confirmed that HSP90 inhibition by 17-AAG markedly accelerated IRF4 degradation in ARP1, RPMI8226, ARH77, and 5TGM1 cells (Figs. 3J and S3J). Importantly, 17-AAG treatment increased K48-linked ubiquitination of IRF4 in ARP1 and RPMI8226 cells (Fig. 3K). Collectively, these results demonstrate that HSP90 stabilizes IRF4 by preventing its ubiquitin-proteasome-mediated degradation, and this protective interaction is disrupted under GD conditions.

Glucose deprivation impairs HSP90-IRF4 interaction through AMPK activation

Given the central role of AMP-activated protein kinase (AMPK) in regulating cellular energy homeostasis [24, 25], we investigated whether AMPK activation mediates GD-induced HSP90 nuclear export and IRF4 degradation. To address this, ARP1 and RPMI8226 cells were treated with A-769662 or metformin (Met), two structurally distinct AMPK activators, at varying concentrations. Both compounds dose-dependently increased AMPK phosphorylation and concurrently reduced IRF4 protein levels (Fig. 4A). Notably, the AMPK inhibitor dorsomorphin (Dorso) completely reversed GD-induced IRF4 loss (Fig. 4B), suggesting AMPK activation is critical for this process. CHX-chase assays demonstrated that AMPK activation by A-769662 or Met significantly accelerated IRF4 degradation (Figs. 4C and 4D), recapitulating the effects of GD or 2-DG treatment. Conversely, AMPK inhibition by Dorso restored IRF4 stability under GD conditions (Figs. 4E and 4F).

Co-IP assays in HA-IRF4-expressing myeloma cells demonstrated that AMPK activation increased K48-linked ubiquitination of IRF4 and disrupted its interaction with HSP90, whereas AMPK inhibition attenuated GD-induced IRF4 ubiquitination and restored the HSP90-IRF4 interaction (Figs. 4G and 4H). Immunofluorescence staining further corroborated these findings: A-769662 or Met treatment mimicked GD-induced nuclear export of HSP90 and reduced HSP90-IRF4 co-localization, while AMPK inhibition largely reversed these effects (Fig. 4I). Notably, GD also triggered nuclear export of ectopically expressed Strep-HSP90 in both ARP1 and HEK293T cells (Figures S4A).

To validate the clinical relevance of these findings, we performed immunohistochemical staining for p-AMPK and IRF4 in myeloma bone marrow biopsies. A strong negative correlation was observed between IRF4 protein levels and p-AMPK levels (Figs. 4J and S4B), supporting our *in vitro* findings that AMPK activation negatively regulates IRF4 stability in myeloma. Taken together, our results demonstrate that metabolic stress-induced AMPK activation drives HSP90 nuclear export and subsequent dissociation from IRF4 (Fig. 4K), establishing AMPK as a promising therapeutic target for modulating IRF4 in multiple myeloma.

TRIM21 is the E3 ligase mediating IRF4 degradation under glucose metabolic stress

In addition to HSP90, our MS analysis identified two E3 ubiquitin ligases, TRIM21 and FBXW11, whose interactions with IRF4 were enhanced under GD conditions (Fig. 3G). To determine whether these ligases regulate IRF4 stability, myeloma cells were transduced with lentiviral shRNAs targeting non-targeted control (sh*Ctrl*), *TRIM21* (sh*TRIM21*), or *FBXW11* (sh*FBXW11*) and cultured under normal glucose or GD conditions. Depletion of *FBXW11* had no effect on IRF4 protein levels under either condition (Figures S5A and S5B), ruling out its role in IRF4 degradation. In contrast, *TRIM21* knockdown did not alter IRF4 levels under normal glucose but significantly attenuated GD-induced IRF4 degradation (Fig. 5A). CHX-chase assays confirmed that *TRIM21* deletion markedly slowed IRF4 degradation under GD conditions (Figs. 5B and 5C). Furthermore, *TRIM21* knockdown abolished, while its overexpression enhanced, GD-induced

K48-linked ubiquitination of IRF4 (Figs. 5D and 5E), establishing TRIM21 as the primary E3 ligase responsible for IRF4 degradation.

Analysis of IRF4 and TRIM21 protein levels in a panel of nine myeloma cell lines revealed a strong negative correlation (Figs. 5F and 5G), further supporting TRIM21's role in negatively regulating IRF4. To elucidate why TRIM21-mediated IRF4 degradation occurs specifically under GD conditions, we performed Co-IP assays to assess IRF4-TRIM21 interactions. GD significantly enhanced IRF4-TRIM21 binding, an effect mimicked by AMPK activation with A-769662 or HSP90 inhibition with 17-AAG (Figs. 5H and 5I). Since AMPK activation disrupts the HSP90-IRF4 interaction, we hypothesized that HSP90 binding to IRF4 sterically hinders TRIM21 access. To test this, HEK293T cells were co-transfected with fixed amounts of Strep-TRIM21 and HA-IRF4 plasmids alongside increasing amounts of Flag-HSP90. Co-IP assays demonstrated that elevated Flag-HSP90 expression progressively weakened the Strep-TRIM21-HA-IRF4 interaction (Fig. 5J), indicating competitive binding between HSP90 and TRIM21 for IRF4.

Structural predictions using AlphaFold suggested that HSP90 and TRIM21 may share a common binding domain on IRF4 (Figure S5C). To map the interaction regions, a series of truncated IRF4 mutants spanning its functional domains were generated (Fig. 5K) and co-expressed with Flag-HSP90 or Strep-TRIM21 in HEK293T cells. Co-IP assays revealed that IRF_{1-420}, IRF_{1-238}, IRF_{1-139}, and $IRF4_{139-238}$ interacted with Strep-TRIM21, while $IRF4_{1-420}$, $IRF4_{1-238}$, $IRF4_{139-238}$, and $IRF4_{238-420}$ bound Flag-HSP90 (Figs. 5L and 5M). These results pinpoint the $IRF4_{139-238}$ (LKD domain) as the shared binding site for both HSP90 and TRIM21. Collectively, these findings support a model in which HSP90 binding to IRF4 under normal glucose conditions blocks TRIM21 access, thereby stabilizing IRF4. Under GD conditions, AMPK activation disrupts the HSP90-IRF4 interaction, exposing IRF4 to TRIM21-mediated ubiquitination and degradation (Fig. 5N).

β-OHB triggers IRF4 acetylation to maintain IRF4 stability under GD conditions

Given that adipocyte-derived β-OHB rescues GD-induced IRF4 reduction, we questioned whether β-OHB maintains IRF4 protein levels through acting on the AMPK-TRIM21 axis. Cycloheximide (CHX)-chase and Co-IP assays revealed that β-OHB treatment restored IRF4 stability (Fig. 6A and S6A), enhanced the IRF4-HSP90 interaction (Fig. 6B), and attenuated GD-induced TRIM21-IRF4 binding (Fig. 6B) and IRF4 K48-linked ubiquitination (Fig. 6C). However, β-OHB did not affect AMPK phosphorylation under GD conditions (Figure S6B), indicating that β-OHB stabilizes IRF4 independently of AMPK signaling.

Since both β-OHB and AcAc protect IRF4 under GD conditions (Fig. 2G), we proposed that β-OHB exerts its effects via the ketolytic pathway, which converts β-OHB and AcAc into acetyl-CoA [26, 27]. To determine whether β-OHB stabilizes IRF4 via acetylation, HA-IRF4-expressing ARP1 cells were treated with or without β-OHB under GD conditions. Cell lysates were immunoprecipitated using anti-HA resin,

separated by SDS-PAGE, and the HA-IRF4 bands were excised for mass spectrometry analysis (Fig. 6D). We identified two putative lysine acetylation sites, K87 and K399, exclusively in β-OHB-treated cells (Fig. 6E). We next mutated each lysine to glutamine (Q), an acetyl-mimetic amino acid, and found that the K87Q mutant, but not K399Q or WT, resisted IRF4 degradation induced by GD or 17-AAG (Fig. 6F and S6C). Moreover, myeloma cells expressing K87Q exhibited greater resistance to GD- or 17-AAG-induced cell death compared to WT or K399Q-expressing cells (Fig. 6G and S6D). K87 of IRF4 is highly conserved across various species (Figure S6E), underscoring its functional importance.

To determine whether K87 acetylation of IRF4 impacts its binding to HSP90 and TRIM21, we performed Co-IP assays using anti-HA resin in ARP1 cells expressing WT, K87Q, or K87R (an acetylation-defective mutant with lysine 87 replaced by arginine). Compared to WT, the K87Q mutant exhibited enhanced binding to HSP90 and reduced interaction with TRIM21 under GD conditions, whereas the K87R (acetyl-defective) mutant abolished these effects (Fig. 6H). Similar results were observed in HEK293T cells co-expressing IRF4 mutants with HSP90 or TRIM21 (Figures S6F and S6G). Notably, 17-AAG, GD or A-769662-stimulated K48-linked ubiquitination of IRF4 was substantially attenuated in K87Q mutant (Fig. 6I). These findings suggest that K87 acetylation of IRF4 enhances its interaction with HSP90, thereby preventing TRIM21-mediated IRF4 degradation under metabolic stress conditions.

To further validate these findings, we designed biotin-conjugated peptides spanning IRF4 residues 74–101, including an acetylated K87 variant (Biotin-K87ac) and an unmodified control (Biotin-K87). Pulldown assays using lysates from HEK293T cells co-expressing Flag-HSP90 and Strep-TRIM21 demonstrated that Biotin-K87ac precipitated significantly more HSP90 but less TRIM21 compared to Biotin-K87 (Figure S6H). These results provide direct biochemical evidence that K87 acetylation enhances IRF4 binding to HSP90 while disrupting its interaction with TRIM21.

We next generated an antibody specific for acetylated K87 and verified its specificity by dot blot assay (Fig. 6J). Using this antibody, we observed that GD treatment reduced IRF4 K87 acetylation in myeloma cells, an effect reversed by β-OHB treatment (Fig. 6J). IHC staining of tumor samples from Fig. 1I revealed reduced IRF4 K87 acetylation in 2-DG-treated tumors, whereas the presence of adipocytes dramatically increased IRF4 K87ac levels (Figs. 6K and 6L). Collectively, these findings suggest that under metabolic stress, myeloma cells exploit adipocyte-derived β-OHB to enhance IRF4 K87 acetylation, thereby stabilizing IRF4 and promoting cell survival.

β-OHB maintains IRF4 stability via OXCT1-mediated ketolysis

To elucidate the mechanism by which β-OHB stabilizes IRF4 under GD conditions, we focused on the ketolysis pathway. Upon cellular uptake, ketone bodies β-OHB and AcAc are catabolized by the mitochondrial enzyme succinyl-CoA:3-ketoacid coenzyme A transferase (OXCT1) [27]. Analysis of two public GEO datasets (GSE2658 and GSE5900) revealed significantly higher *OXCT1* expression in malignant plasma cells from myeloma patients compared to normal plasma cells from healthy donors (Figure S7A). Furthermore, analysis of the Multiple Myeloma Research Foundation (MMRF)-CoMMpass

database (n = 859) using the UCSC Xena platform (http://xena.ucsc.edu/) demonstrated that high *OXCT1* expression correlated with poor overall survival in myeloma patients (Figure S7B), suggesting a potential oncogenic role for OXCT1.

Using pimozide, an OXCT1 inhibitor, to block β-OHB catabolism [28], we showed OXCT1 inhibition abrogated the ability of β-OHB to restore IRF4 stability and cell viability under GD conditions (Figures S7C-S7E), indicating that β-OHB exerts its protective effects through mitochondrial ketolysis. To elucidate the role of OXCT1-mediated β-OHB metabolism *in vivo*, we implemented an alternate-day fasting (ADF) regimen in C57BL/6J mice to induce metabolic stress and elevate systemic ketone body levels. After one week of ADF, mice were inoculated with Vk12598 cells and treated with pimozide (Figure S7F). ADF significantly increased serum ketone body levels, while pimozide reduced ketone body concentrations in both control and ADF mice (Figure S7G). Notably, both ADF and pimozide treatment alone effectively suppressed myeloma tumor burden, as evidenced by decreased serum M-protein levels, reduced spleen and liver sizes, and improved survival (Figures S7H-S7J). The combination of ADF and pimozide further enhanced these effects, suggesting that OXCT1-mediated β-OHB catabolism fuels myeloma cell survival under metabolic stress.

Using the UCSC Xena platform, we identified a positive correlation between *OXCT1* and *IRF4* mRNA levels (Figure S8A). To explore the transcriptional regulation of *OXCT1*, we employed Cistrome, hTFtarget, and chEA3 tools, identifying 24 potential transcription factors (TFs) for OXCT1, including IRF4 (Figure S8B). Subsequent cleavage under targets and tagmentation (CUT & Tag) analysis revealed that IRF4 binding was enriched at transcription start sites (TSSs) of protein-coding genes, with reduced binding under GD conditions that was restored by β-OHB treatment (Figure S8C). Specifically, IRF4 binding at the *OXCT1* promoter decreased under GD exposure but was rescued by β-OHB (Figure S8D).

To validate direct transcriptional regulation, we cloned a 2.0 kb *OXCT1* promoter region upstream of a luciferase reporter gene (pGL2-*OXCT1*) and co-transfected it with either GFP or HA-IRF4 plasmids into HEK293T cells. Overexpression of HA-IRF4 significantly increased luciferase activity compared to the GFP control (Figure S8E), indicative of a direct transcription regulation of *OXCT1* by IRF4 protein. Interestingly, we also observed positive correlations between *OXCT1* mRNA levels and known IRF4 target genes, including *E2F5*, *STAG2*, *MYC*, *PIM2*, *SCL37A4*, *USB1*, *CASP3* and *CANX* (Figures S8G-S8N). Collectively, these findings suggest a positive feedback loop in myeloma cells, wherein OXCT1-mediated β-OHB metabolism sustains IRF4 stability, while IRF4 transcriptionally upregulates OXCT1 expression (Figure S8F).

NAT10 mediates β-OHB-induced IRF4 K87 acetylation

To identify the acetyltransferase responsible for β-OHB-induced IRF4 K87 acetylation, we screened a panel of inhibitors targeting major acetyltransferases (p300, CBP, PCAF, GCN5, KAT8, and NAT10) in myeloma cells under GD conditions with β-OHB treatment. Notably, both the KAT2B inhibitor NSC 694623 and the NAT10 inhibitor Remodelin abolished β-OHB-mediated protection of IRF4 stability

(Fig. 7A) and cell viability (Fig. 7B) in ARP1 cells. Subsequent co-IP assays in HEK293T cells co-expressing IRF4-GFP with either HA-KAT2B or Flag-NAT10 revealed that NAT10, but not KAT2B, physically interacted with IRF4 (Fig. 7C). Consistently, Remodelin (but not NSC 694623) significantly attenuated β-OHB-induced IRF4 K87 acetylation (Fig. 7D), establishing NAT10 as the primary acetyltransferase mediating this modification.

Genetic validation was achieved through *NAT10* knockout in ARP1 cells, which demonstrated that β-OHB's protective effects on IRF4 protein stability and cell viability during metabolic stress are strictly NAT10-dependent (Figs. 7E and 7F). Supporting this functional relationship, we found significant positive correlations between NAT10 expression levels and those of established IRF4 transcriptional targets (Figures S9A-S9H), implying NAT10 may regulate IRF4 activity. To assess clinical relevance, we analyzed GEO datasets (GSE2658 and GSE5900) and observed markedly higher NAT10 expression in malignant plasma cells versus normal controls (Fig. 7G). Importantly, elevated NAT10 expression strongly predicted worse clinical outcomes in myeloma patients (Fig. 7H), positioning NAT10 as both a promising therapeutic target and a potential prognostic biomarker for multiple myeloma.

Synergistic anti-myeloma effects of AMPK activation and NAT10/OXCT1 inhibition

Given that β-OHB protects IRF4 stability and cell survival independently of AMPK pathway (Fig. 7N), we investigated whether combined AMPK activation and NAT10 inhibition exerts synergistic anti-myeloma effects. To this end, we employed an inhibitor matrix in ARP1 cells to evaluate multiple combinatorial concentrations of Metformin with either Remodelin or Pimozide. Quantitative synergy analysis using SynergyFinder 3.0 [29] demonstrated strong synergistic interactions for both combinations, with ZIP synergy scores of 24.279 for Metformin-Remodelin and 22.137 for Metformin-Pimozide (Figs. 7I and 7J).

To validate these findings *in vivo*, we inoculated C57BL/6J mice with murine Vk12598 cells and treated them with Metformin, Pimozide, or Remodelin as monotherapies or in combination. While single-agent treatments elicited modest anti-tumor effects, combined Metformin-Pimozide or Metformin-Remodelin therapy significantly suppressed myeloma progression. This was evidenced by marked reductions in serum M-protein levels, diminished tumor infiltration in spleens and livers, and prolonged survival (Figs. 7K-7M). In summary, our study demonstrates that dual targeting of AMPK activation alongside NAT10 or OXCT1 inhibition elicits potent synergistic anti-myeloma activity (Fig. 7N).

DISCUSSION

Our study elucidates a sophisticated metabolic crosstalk between adipocytes and myeloma cells, uncovering novel mechanisms of tumor cell adaptation to nutrient stress. We demonstrate that glucose deprivation activates AMPK signaling, which disrupts the protective HSP90-IRF4 interaction, thereby exposing IRF4 to TRIM21-mediated ubiquitination and subsequent proteasomal degradation. Paradoxically, metabolic stress simultaneously induces adipocyte-derived-β-OHB secretion, which

undergoes OXCT1-mediated ketolysis in myeloma cells to promote NAT10-dependent acetylation of IRF4 at K87. This acetylation event restores HSP90-IRF4 binding, effectively shielding IRF4 from degradation and sustaining myeloma cell survival (Fig. 7N).

While ketone bodies have traditionally been recognized as energy substrates shuttled from the liver to peripheral tissues during fasting or exercise, emerging evidence reveals their production in extrahepatic tissues where they function as autocrine/paracrine signaling molecules [30, 31]. Notably, adipocytes have been identified as a significant extrahepatic ketone source during β-adrenergic stimulation or cold exposure [32]. Our work extends these findings by demonstrating that alternate-day fasting (ADF) induces browning of white adipose tissue, concomitant with upregulation of ketogenic enzymes and enhanced ketone body production. Genetic ablation of *Hmgcs2*, the rate-limiting ketogenesis enzyme, in adipocytes completely abrogates their pro-survival effects on myeloma cells under metabolic stress, establishing adipocyte-derived ketone bodies as crucial paracrine mediators of myeloma cell viability.

Most tumors preferentially rely on aerobic glycolysis to meet their heightened bioenergetic and biosynthetic demands, a metabolic vulnerability that can be therapeutically targeted through glucose restriction [33]. Intermittent fasting has emerged as a promising intervention to lower systemic glucose availability and impair tumor glycolytic metabolism [14]. Preclinical studies demonstrate its efficacy both as monotherapy and in combination with conventional treatments across various malignancies [15, 34, 35]. The anti-tumor effects of intermittent fasting appear to be mediated through two mechanisms: systemic glucose restriction and ketone body generation. Although β-OHB has been shown to enhance $CD8^+$ T cell anti-tumor immunity [36] and suppress colorectal cancer progression via the Hcar2 receptor [37], its role appears context-dependent. Notably, ketogenic interventions have been associated with adverse effects, including accelerated cachexia [38] and exacerbated chemotherapy toxicity [39], underscoring the need for careful evaluation of ketone metabolism in cancer therapy.

Our study reveals a paradoxical pro-tumorigenic role of β-OHB in multiple myeloma under ADF conditions. Although ADF itself exerts potent anti-myeloma effects, the concomitant elevation of systemic ketone bodies supports tumor survival through OXCT1-dependent ketolysis. Pharmacological inhibition of OXCT1 synergizes with ADF, further suppressing tumor growth and prolonging survival in myeloma-bearing mice. OXCT1, the rate-limiting enzyme of ketone catabolism, is highly expressed in myeloma cells and correlates with poor patient prognosis. These findings establish ketolysis as a critical metabolic adaptation that sustains myeloma cell survival under fasting conditions and highlight OXCT1 as a promising therapeutic target. While intermittent fasting retains considerable therapeutic potential, our findings underscore the need for context-specific evaluation, as fasting-induced ketogenesis may inadvertently fuel tumor progression in certain malignancies.

IRF4, a master transcriptional regulator, orchestrates diverse gene networks essential for myeloma cell proliferation, survival, and metabolism. Genetic ablation of IRF4 is universally lethal across myeloma subtypes regardless of their genetic background, establishing it as a compelling therapeutic target [40].

Our previous work revealed that ACSS2 inhibition triggers p62-dependent lysosomal degradation of IRF4, suppressing myeloma growth, thereby positioning ACSS2 as a promising target for IRF4-directed therapy [9]. Here, we unveil a novel dual-layer ubiquitin-proteasome regulatory system governing IRF4 protein homeostasis: (1) Under glucose-replete conditions, HSP90 stabilizes IRF4 by sterically shielding it from recognition by the E3 ubiquitin ligase TRIM21. Glucose deprivation, however, activates AMPK, disrupting the HSP90-IRF4 interaction and exposing IRF4 to TRIM21-mediated ubiquitination and proteasomal degradation. (2) Conversely, adipocyte-derived β-OHB sustains IRF4 stability via OXCT1-dependent ketolysis, enabling NAT10-mediated K87 acetylation to restore HSP90 binding under metabolic stress. This dynamic interplay between degradation (AMPK-TRIM21 axis) and salvage (β-OHB-OXCT1-NAT10 axis) pathways highlights myeloma's metabolic adaptability and expands opportunities for IRF4-targeted therapy.

To bridge our mechanistic findings with potential clinical applications, we evaluated the synergistic antimyeloma effects of AMPK activation (via metformin) combined with OXCT1 or NAT10 inhibition (using Remodelin or Pimozide, respectively), all FDA-approved agents with well-characterized mechanisms [41–43]. Notably, the combination of metformin with either Remodelin or Pimozide exhibited potent, synergistic antimyeloma activity and prolonged survival in preclinical models. Given the re-entry of the glycolysis inhibitor 2-DG into clinical trials, our findings support the rationale for combining glycolysis inhibitors, intermittent fasting regimens, or AMPK activators with OXCT1 or NAT10 inhibitors as a novel antimyeloma strategy.

Collectively, our findings have shed light on a mechanistic insight into the roles of adipocytes in myeloma metabolic stress resistance. Metabolic stressors, such as intermittent fasting, glycolysis inhibitor, or AMPK activator, may suppress myeloma progression by inducing IRF4 proteasomal degradation. Conversely, metabolic stress also stimulates adipocytes to produce ketone bodies, which counteract IRF4 degradation and sustain myeloma cell survival under nutrient deprivation. These findings unveil a novel therapeutic paradigm by combining metabolic stress induction with ketolysis inhibition, offering a promising avenue for improving myeloma treatment outcomes.

Declarations

Declaration of Interests:

The authors declare no potential conflicts of interest.

Author Contributions:

C.S., P.Y., Y.L., T.X., W.W., H.L. and Z.L. designed all experiments and wrote the manuscript; C.S., P.Y., Y.L., T.X, R.L., W.L., T.J., J.L., Q.W., and Y.Y. performed experiments and statistical analyses; W.W. and Y.W.

provided patient samples; R.L. and B.X. performed bioinformatics analysis; CF.L provided critical suggestions.

Acknowledgements

This work was supported by the National Natural Science Foundation of China (No. 82270217) and the Postgraduate Innovation Research and Practice Program of Anhui Medical University (No. YJS20230145 & YJS20240076). We are deeply grateful to Dr. P. Leif Bergsagel (Division of Hematology and Medical Oncology, Mayo Clinic, USA) for generously providing the Vk12598 cell line.

References

1. Kyle, R.A. & Rajkumar, S.V. Multiple myeloma. N Engl J Med 351, 1860–1873 (2004).
2. Seiden, M.V. & Anderson, K.C. Multiple myeloma. Curr Opin Oncol 6, 41–49 (1994).
3. Lauby-Secretan, B. *et al.* Body Fatness and Cancer–Viewpoint of the IARC Working Group. N Engl J Med 375, 794–798 (2016).
4. Lichtman, M.A. Obesity and the risk for a hematological malignancy: leukemia, lymphoma, or myeloma. Oncologist 15, 1083–1101 (2010).
5. Sonderman, J.S. *et al.* Multiple Myeloma Mortality in Relation to Obesity Among African Americans. J Natl Cancer Inst 108 (2016).
6. Ambrosi, T.H. *et al.* Adipocyte Accumulation in the Bone Marrow during Obesity and Aging Impairs Stem Cell-Based Hematopoietic and Bone Regeneration. Cell Stem Cell 20, 771–784 (2017).
7. Luo, Y. *et al.* Microbiota from Obese Mice Regulate Hematopoietic Stem Cell Differentiation by Altering the Bone Niche. Cell Metabolism 22, 886–894 (2015).
8. Liu, H. *et al.* Reprogrammed marrow adipocytes contribute to myeloma-induced bone disease. Science Translational Medicine 11 (2019).
9. Li, Z.W. *et al.* Acetyl-CoA Synthetase 2: A Critical Linkage in Obesity-Induced Tumorigenesis in Myeloma. Cell Metabolism 33, 78-+ (2021).
10. Morris, E.V. & Edwards, C.M. Adipokines, adiposity, and bone marrow adipocytes: Dangerous accomplices in multiple myeloma. Journal of Cellular Physiology 233, 9159–9166 (2018).
11. Hanahan, D. & Weinberg, R.A. Hallmarks of Cancer: The Next Generation. Cell 144, 646–674 (2011).
12. Schulze, A. & Harris, A.L. How cancer metabolism is tuned for proliferation and vulnerable to disruption. Nature 491, 364–373 (2012).
13. Thandapani, P. *et al.* Valine tRNA levels and availability regulate complex I assembly in leukaemia. Nature 601, 428–433 (2022).
14. Nencioni, A., Caffa, I., Cortellino, S. & Longo, V.D. Fasting and cancer: molecular mechanisms and clinical application. Nature Reviews Cancer 18, 707–719 (2018).

15. Elgendy, M. *et al.* Combination of Hypoglycemia and Metformin Impairs Tumor Metabolic Plasticity and Growth by Modulating the PP2A-GSK3β-MCL-1 Axis. Cancer Cell 35, 798-+ (2019).
16. Zhu, Z.J., Jiang, W.P., McGinley, J.N. & Thompson, H.J. 2-Deoxyglucose as an energy restriction mimetic agent:: Effects on mammary carcinogenesis and on mammary tumor cell growth. Cancer Research 65, 7023–7030 (2005).
17. Kumar, A. *et al.* 2-Deoxyglucose drives plasticity via an adaptive ER stress-ATF4 pathway and elicits stroke recovery and Alzheimer's resilience. Neuron 111, 2831–2846 (2023).
18. Ambrosi, T.H. *et al.* Adipocyte Accumulation in the Bone Marrow during Obesity and Aging Impairs Stem Cell-Based Hematopoietic and Bone Regeneration. Cell Stem Cell 20, 771-+ (2017).
19. Shaffer, A.L. *et al.* IRF4 addiction in multiple myeloma. Nature 454, 226–231 (2008).
20. Bendridi, N., Selmi, A., Balcerczyk, A. & Pirola, L. Ketone Bodies as Metabolites and Signalling Molecules at the Crossroad between Inflammation and Epigenetic Control of Cardiometabolic Disorders. International Journal of Molecular Sciences 23 (2022).
21. Miyamoto, J. *et al.* Ketone body receptor GPR43 regulates lipid metabolism under ketogenic conditions. Proceedings of the National Academy of Sciences of the United States of America 116, 23813–23821 (2019).
22. Fabbiano, S. *et al.* Caloric Restriction Leads to Browning of White Adipose Tissue through Type 2 Immune Signaling. Cell Metabolism 24, 434–446 (2016).
23. Martínez-Férriz, A., Ferrando, A., Fathinajafabadi, A. & Farràs, R. Ubiquitin-mediated mechanisms of translational control. Seminars in Cell & Developmental Biology 132, 146–154 (2022).
24. Herzig, S. & Shaw, R.J. AMPK: guardian of metabolism and mitochondrial homeostasis. Nature Reviews Molecular Cell Biology 19, 121–135 (2018).
25. Penugurti, V., Manne, R.K., Bai, L., Kant, R. & Lin, H.K. AMPK: The energy sensor at the crossroads of aging and cancer. Seminars in Cancer Biology 106, 15–27 (2024).
26. Nelson, A.B., Queathem, E.D., Puchalska, P. & Crawford, P.A. Metabolic Messengers: ketone bodies. Nature Metabolism 5, 2062–2074 (2023).
27. Newman, J.C. & Verdin, E. Ketone bodies as signaling metabolites. Trends in Endocrinology and Metabolism 25, 42–52 (2014).
28. Zhu, C.X. *et al.* Targeting OXCT1-mediated ketone metabolism reprograms macrophages to promote antitumor immunity via CD8 + T cells in hepatocellular carcinoma. J Hepatol 81, 690–703 (2024).
29. Ianevski, A., Giri, A.K. & Aittokallio, T. SynergyFinder 3.0: an interactive analysis and consensus interpretation of multi-drug synergies across multiple samples. Nucleic Acids Research 50, W739-W743 (2022).
30. Silva, B. *et al.* Glia fuel neurons with locally synthesized ketone bodies to sustain memory under starvation. Nat Metab 4, 213–224 (2022).
31. Cheng, C.W. *et al.* Ketone Body Signaling Mediates Intestinal Stem Cell Homeostasis and Adaptation to Diet. Cell 178, 1115–1131 e1115 (2019).

32. Wang, W. *et al.* A PRDM16-Driven Metabolic Signal from Adipocytes Regulates Precursor Cell Fate. Cell Metab 30, 174–189 e175 (2019).
33. Pavlova, N.N. & Thompson, C.B. The Emerging Hallmarks of Cancer Metabolism. Cell Metabolism 23, 27–47 (2016).
34. Gallage, S. *et al.* A 5:2 intermittent fasting regimen ameliorates NASH and fibrosis and blunts HCC development via hepatic PPAR a and PCK1. Cell Metabolism 36 (2024).
35. Lien, E.C. *et al.* Low glycaemic diets alter lipid metabolism to influence tumour growth. Nature 599, 302–307 (2021).
36. Luda, K.M. *et al.* Ketolysis drives CD8 + T cell effector function through effects on histone acetylation. Immunity 56, 2021-+ (2023).
37. Dmitrieva-Posocco, O. *et al.* β-Hydroxybutyrate suppresses colorectal cancer. Nature 605, 160-+ (2022).
38. Ferrer, M. *et al.* Ketogenic diet promotes tumor ferroptosis but induces relative corticosterone deficiency that accelerates cachexia. Cell Metabolism 35 (2023).
39. Ozcan, M. *et al.* Sustained alternate-day fasting potentiates doxorubicin cardiotoxicity. Cell Metab 35, 928–942 e924 (2023).
40. Shaffer, A.L. *et al.* IRF4 addiction in multiple myeloma. Nature 454, 226–231 (2008).
41. Ma, T. *et al.* Low-dose metformin targets the lysosomal AMPK pathway through PEN2. Nature 603, 159–165 (2022).
42. Al Batran, R. *et al.* Pimozide Alleviates Hyperglycemia in Diet-Induced Obesity by Inhibiting Skeletal Muscle Ketone Oxidation. Cell Metab 31, 909–919 e908 (2020).
43. Balmus, G. *et al.* Targeting of NAT10 enhances healthspan in a mouse model of human accelerated aging syndrome. Nat Commun 9, 1700 (2018).

Figures

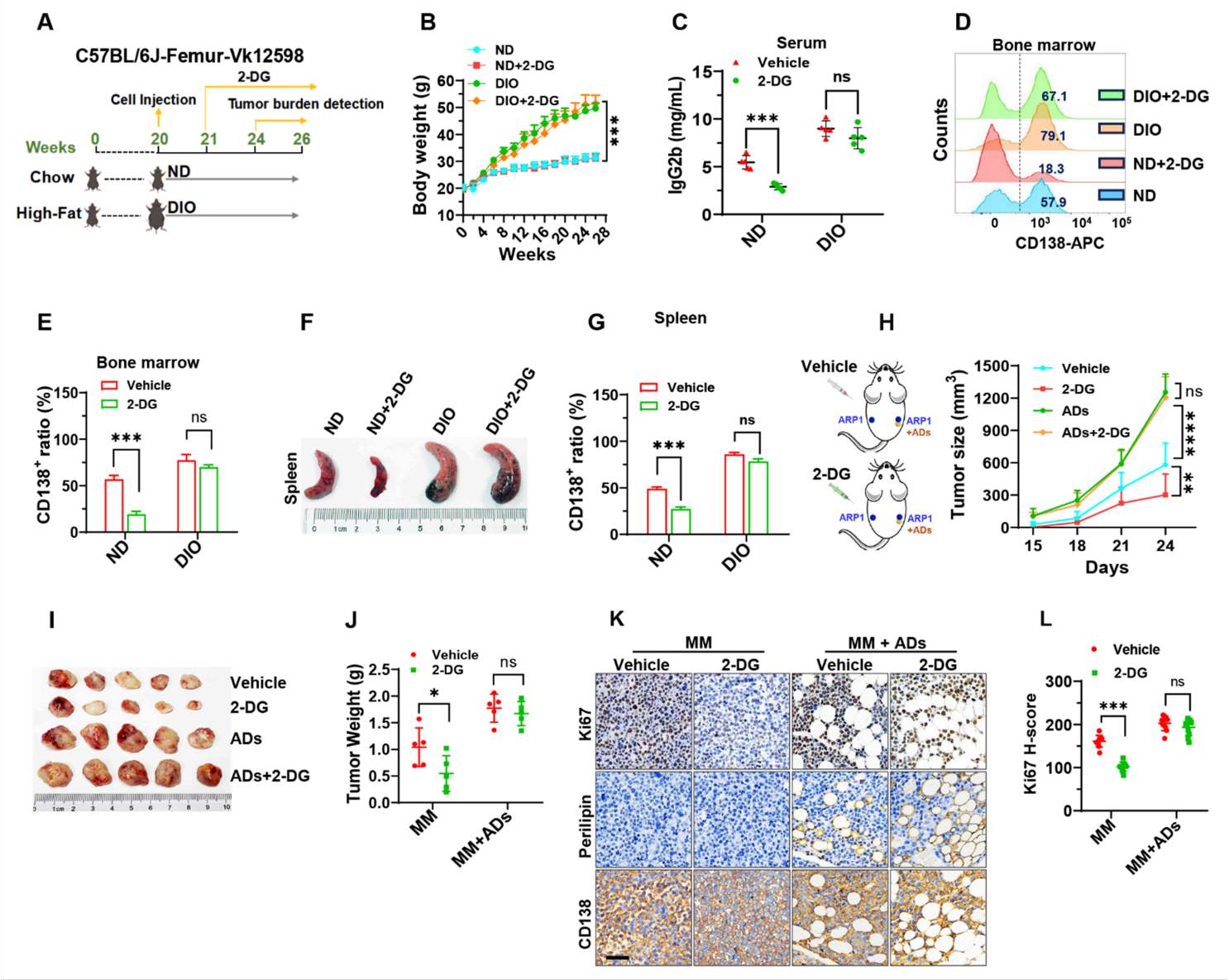


Figure 1

Adipocytes promote myeloma cell resistance to 2-DG-induced metabolic stress *in vivo*

(A-G) Male C57BL/6J mice (6 weeks old, n=5/group) were fed a high-fat diet (DIO) or normal diet (ND) for 20 weeks, followed by intrafemoral injections of Vk12598 murine myeloma cells (2×10^6 cells/mouse). 2-DG intervention commenced one week post-tumor inoculation (5 weeks duration). (A) Experimental timeline. (B) Body weight changes over time. (C) Serum IgG2b levels quantified by ELISA. (D) Representative flow cytometry plots showing gated $CD138^+$ myeloma populations from bone marrow samples. (E) Quantitative analysis of $CD138^+$ cell frequencies across experimental groups. (F) Representative images of spleens from each group. (G) Percentage of $CD138^+$ myeloma cells in the spleen. (H-L) ARP1 cells (2×10^5 cells/site), either alone or co-injected with human MSC-derived adipocytes (5×10^5 cells/site), were subcutaneously implanted into the left or right flank of NCG mice, respectively. Mice were treated with 2-DG (500 mg/kg, i.p.) starting 1 week post-injection. (H) Schematic

of injection sites (left) and tumor growth curves (right). (I) Representative images of excised tumors at endpoint (4 weeks). (J) Tumor weights. (K) Immunohistochemical staining of tumor tissues for Ki67, CD138, and perilipin. Scale bars: 100 μm. (L) Quantification of Ki67 expression (H-score). Data are presented as mean ± SD (n=5 mice/group) and are representative of two independent experiments. Statistical significance was determined by two-way ANOVA with Bonferroni's post hoc test (B, C, E, G, H, J, L). *Ns*, not significant; *P < 0.05; **P < 0.01; ***P < 0.001; ****P < 0.0001. See also Figure S1.

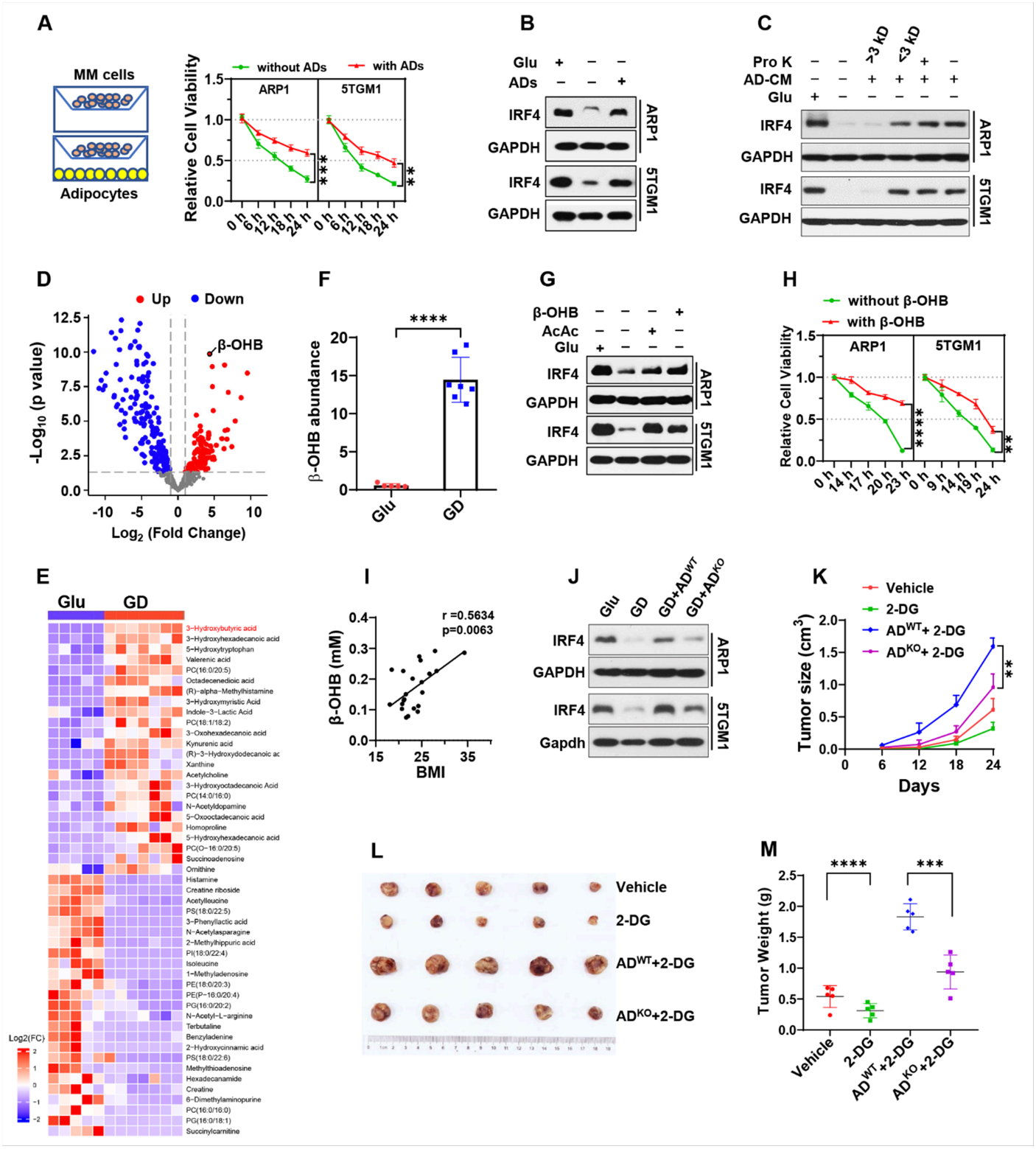
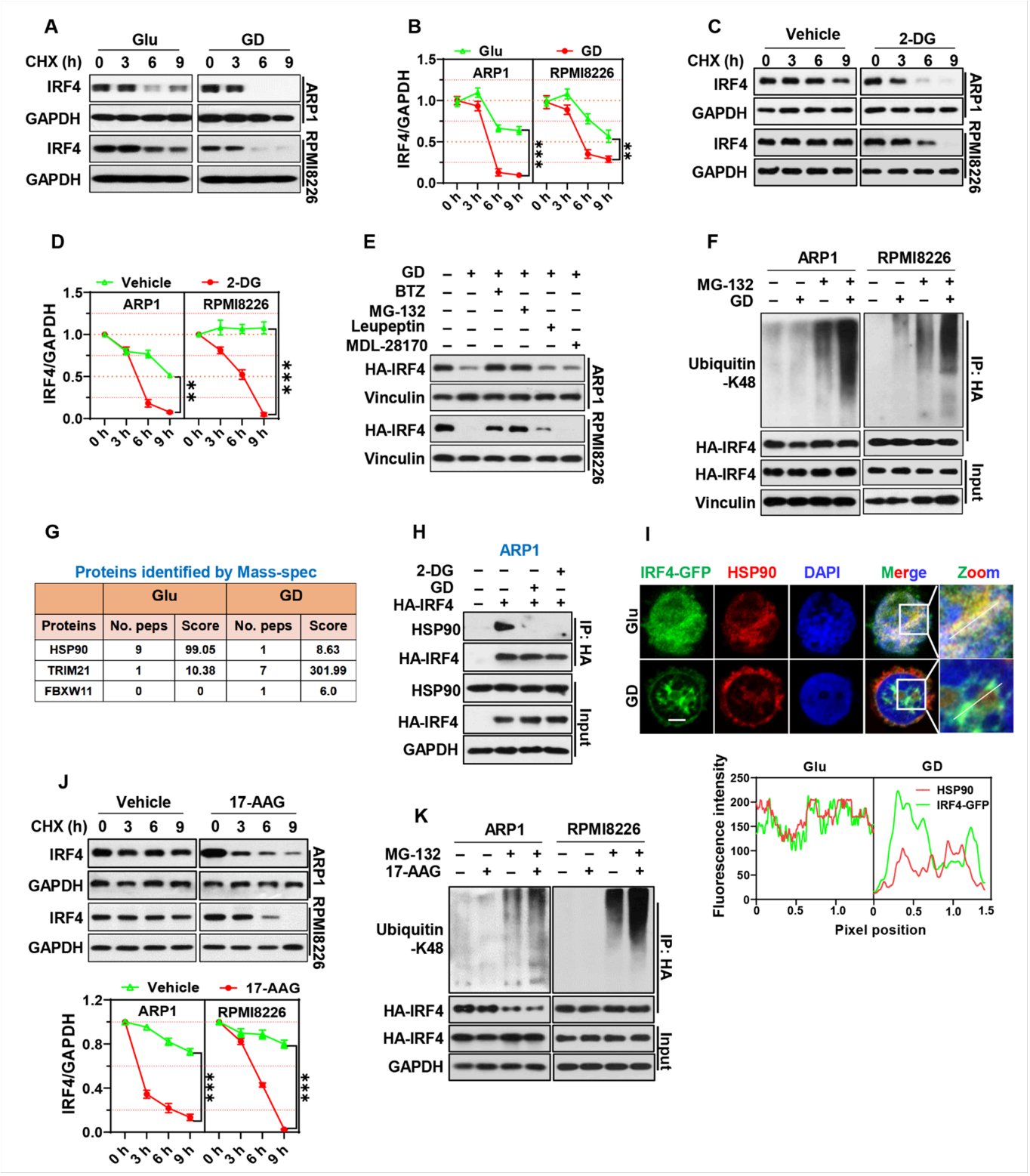


Figure 2

Adipocyte-derived β-OHB promotes myeloma cell resistance to GD *in vitro* and *in vivo*

(A) Coculture of myeloma cells with adipocytes under GD conditions. Left: Schematic of transwell coculture system using human MSC-derived adipocytes with ARP1 cells or murine OP9-derived adipocytes with 5TGM1 cells. Right: Time-course viability of myeloma cells with or without adipocyte coculture under GD conditions. (B) Western blot analysis of IRF4 expression in ARP1 and 5TGM1 cells after 16-hour coculture with adipocytes under GD conditions. (C) Western blot analysis of IRF4 expression in myeloma cells treated with AD-CM under GD conditions. AD-CM was collected from adipocytes cultured under GD and subjected to: (1) no treatment, (2) Proteinase K digestion, or (3) size fractionation (<3 kDa or >3 kDa). (D-F) Metabolomic analysis of AD-CM under GD vs normal glucose. (D) Volcano plot of differentially abundant metabolites. (E) Heatmap of top regulated metabolites. (F) Relative abundance of β-OHB in AD-CM under GD vs normal glucose. (G) Western blot analysis of IRF4 expression in myeloma cells treated with β-OHB or AcAc under GD conditions for 16 h. (H) Time-course viability of myeloma cells with or without β-OHB under GD conditions. (I) Correlation between bone marrow β-OHB levels and patients' BMIs. (J) Western blot analysis of IRF4 expression in myeloma cells following coculture with adipocytes. Myeloma cells were cocultured for 16 h under GD conditions using a transwell system with adipocytes isolated from either *Hmgcs2*^{WT} (AD^{WT}) or *Hmgcs2*^{AKO} (AD^{KO}) mice. Prior to coculture, adipocytes were subjected to 24-hour GD pretreatment. (K-M) 5TGM1 cells (2×10^6 cells/site) were injected subcutaneously into the left or right flank of nude mice either alone or premixed with an equal number of AD^{WT} or AD^{KO} adipocytes. Mice received 2-DG treatment starting 1 week post-injection, and tumor volumes were measured weekly. After 4 weeks, tumors were harvested for analysis. (K) Tumor growth curves. (L) Representative images of excised tumors. (M) Quantitative analysis of tumor weights. Data shown as mean ± SD were representative of three independent experiments. *P < 0.05; **P < 0.01; ***P < 0.001; ****P < 0.0001. Statistical significance was determined using a two-tailed Student's t-test (F, M) or two-way ANOVA with Bonferroni's post hoc test (A, H, K). See also Figure S2.



	Glu		GD	
Proteins	No. peps	Score	No. peps	Score
HSP90	9	99.05	1	8.63
TRIM21	1	10.38	7	301.99
FBXW11	0	0	1	6.0

Figure 3

GD promotes IRF4 degradation via disruption of IRF4-HSP90 interaction.

(A) Time-course of IRF4 protein levelsin ARP1 and RPMI8226 cells treated with 100 μg/mL cycloheximide (CHX) under normal glucose or GD. (B) Quantification of IRF4 protein normalized to GAPDH (corresponding to A). (C) IRF4 protein kinetics in myeloma cells treated with or without 10 mM 2-

DG in the presence of CHX. (D) Quantified IRF4 protein normalized to GAPDH (corresponding to C). (E) IRF4 protein levels in myeloma cells after 16-hour GD treatment in the presence or absence of 1 μM MG-132, 50 nM bortezomib (BTZ), 10 μM leupeptin, or 1 μM MDL-28170. (F) Cell lysates were prepared from HA-IRF4-expressing myeloma cells following 16-hour GD treatment, with 1 μM MG-132 added for the final 6 hours to prevent proteasomal degradation. Lysates were immunoprecipitated using anti-HA affinity resin and subsequently immunoblotted with antibodies specific for K48-linked ubiquitin chains and HA-IRF4. (G) Mass spectrometry analysis of HA-IRF4 immunoprecipitates from RPMI8226 cells cultured under normal glucose or GD conditions. Proteins were pulled down using anti-HA resin, and identified interactors are listed in the table. (H) Co-immunoprecipitation (Co-IP) of HA-IRF4 with endogenous HSP90 in HA-IRF4-expressing ARP1 cells under GD or 2-DG treatment. Lysates were immunoprecipitated with anti-HA resin and immunoblotted for HA and HSP90. (I) Colocalization analysis of IRF4-GFP and HSP90. (Upper) Representative confocal microscopy images showing spatial distribution of IRF4-GFP (green) and endogenous HSP90 (red) under normal glucose or GD conditions, with DAPI-stained nuclei (blue). (Lower) Fluorescence intensity quantification of the demarcated regions (white lines) using ImageJ software, demonstrating colocalization characteristics between the two channels. Scale bar: 5 μm. (J) Time-course of IRF4 protein levels in myeloma cells following treatment with 100 μg/mL CHX with or without 2 μM 17-AAG (upper). Quantification of IRF4 protein levels normalized to GAPDH (lower). (K) Myeloma cells expressing HA-IRF4 were treated with or without 17-AAG for 16 h with 1 μM MG-132 added for the final 6 hours, followed by HA immunoprecipitation and immunoblotting for K48-ubiquitin and HA-IRF4. Data shown as mean ± SD were representative of three independent experiments. **P < 0.01; ***P < 0.001. P values were determined by two-way ANOVA with Bonferroni's post hoc test (B, D and J). See also Figure S3.

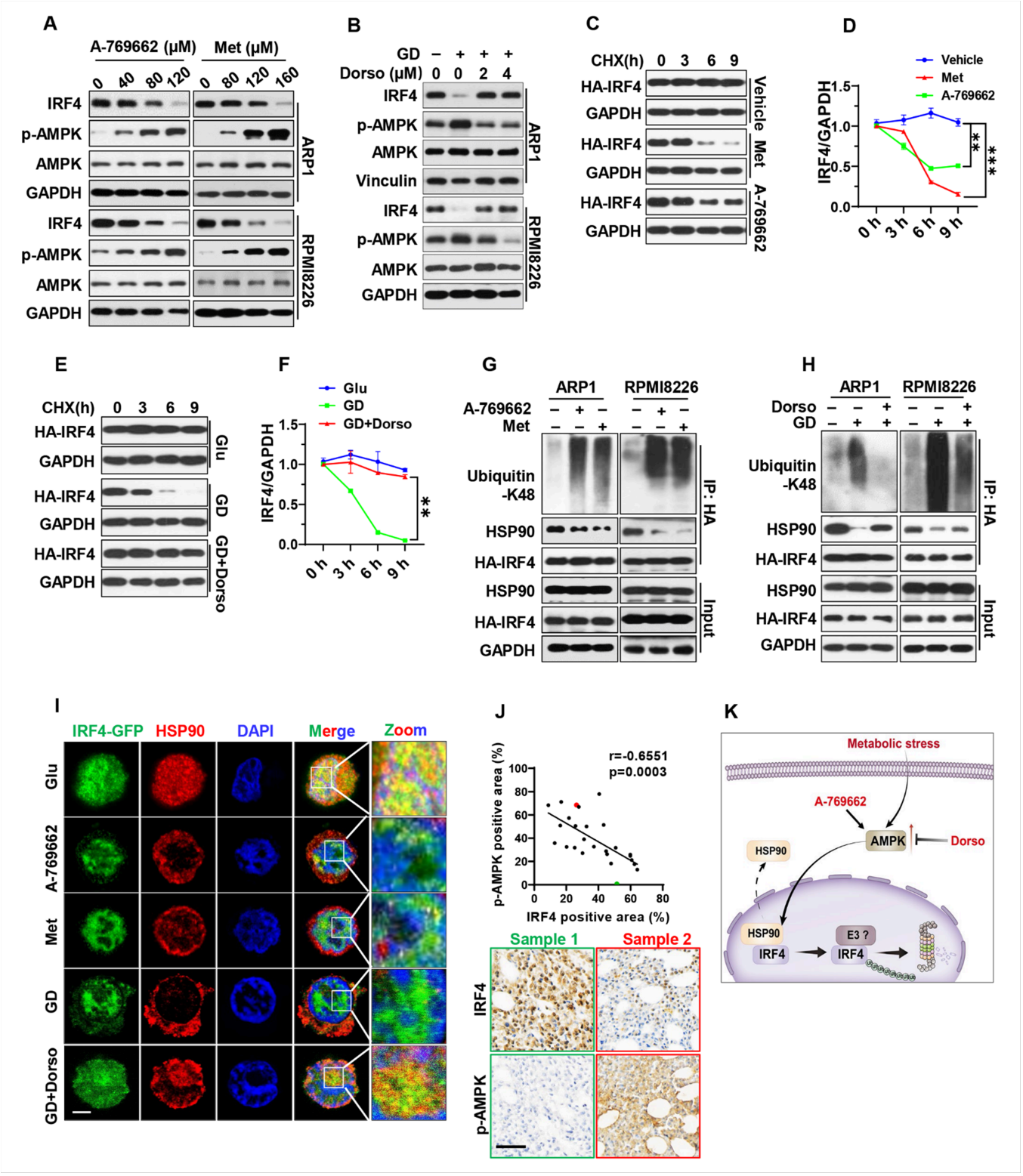


Figure 4

Glucose deprivation impairs HSP90-IRF4 interaction through AMPK activation.

(A) Immunoblot analysis of IRF4, p-AMPK, and total AMPK in myeloma cells treated with A-769662 or metformin (Met) at indicated doses for 16 h. (B) Immunoblot analysis of IRF4, p-AMPK, and AMPK in myeloma cells under normal glucose or GD treated with or without dorsomorphin (Dorso) for 16 h. (C)

Immunoblot of HA-IRF4 in HA-IRF4-expressing ARP1 and RPMI8226 cells treated with CHX plus A-769662 or Met. (D) Quantification of HA-IRF4 protein levels normalized to GAPDH (corresponding to C). (E) Degradation kinetics of HA-IRF4 in ARP1 cells treated with Dorso (4 μM) and CHX (100 μg/mL) under GD conditions. (F) Quantification of HA-IRF4 protein levels normalized to GAPDH. (G) Co-IP of HA-IRF4 with endogenous HSP90 in cells treated with A-769662 or Met for 16 h. Immunoblotting was detected with antibodies against K48-ubiquitin, HA or HSP90. (H) Co-IP of HA-IRF4 with endogenous HSP90 in cells under normal glucose or GD conditions with or without Dorso treatment for 16 h. Immunoblotting was detected with antibodies against K48-ubiquitin, HA or HSP90. (I) Representative immunofluorescence of IRF4-GFP (green) and endogenous HSP90 (red) in cells treated with A-769662, Met, GD or GD+Dorso. Nuclei were stained with DAPI (blue). Scale bar: 5 μm. (J) Upper: Correlation between p-AMPK and IRF4 levels in myeloma patients' bone marrow biopsies. Lower: Representative immunohistochemistry for IRF4 and p-AMPK, corresponding to the red and green data points in panel J. (K) Proposed Model: Metabolic stress activates AMPK, resulting in HSP90 nuclear export and disrupting HSP90-IRF4 interaction. Data are mean ± SD from three independent experiments. **P < 0.01, ***P < 0.001 by two-way ANOVA with Bonferroni post-test (D, F). See also Figure S4.

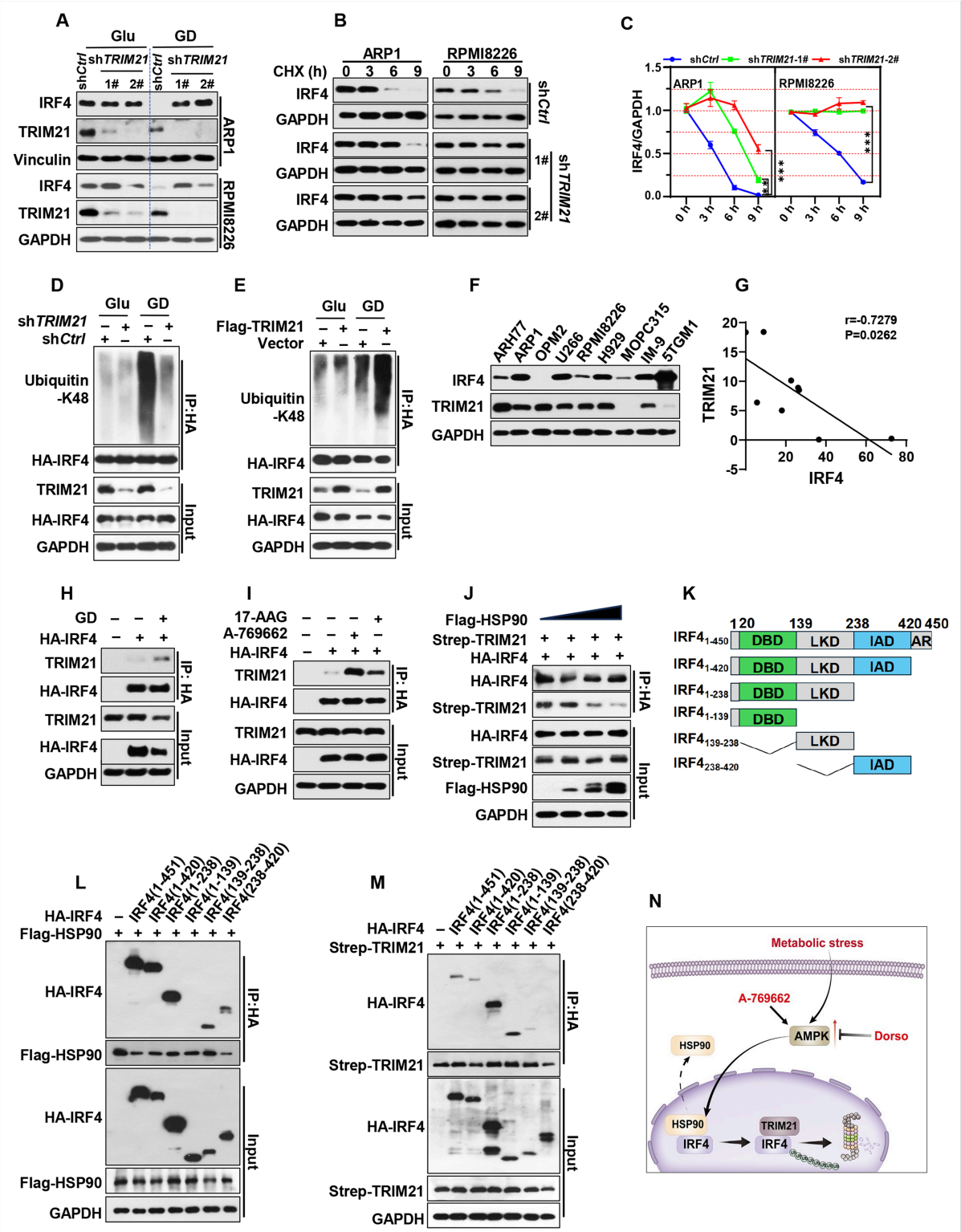


Figure 5

TRIM21 mediates IRF4 degradation under glucose metabolic stress

(A)Immunoblot analysis of IRF4 and TRIM21 protein levels in ARP1 or RPMI8226 cells expressing sh*Ctrl*, sh*TRIM21*-1, or sh*TRIM21*-2, under normal glucose or GD conditions. (B-C) Time-course analysis of IRF4 protein levels in sh*Ctrl*-, sh*TRIM21*-1-, or sh*TRIM21*-2-expressing cells treated with 100 μg/mL CHX (B).

Quantification of normalized IRF4 levels relative to GAPDH is shown (C). (D) HA-IRF4-expressing ARP1 cells were infected with sh*Ctrl* or sh*TRIM21* and cultured under GD conditions for 16 h. Anti-HA immunoprecipitates were probed for K48- ubiquitin and HA-IRF4. Inputs are shown as controls. (E) HA-IRF4-expressing ARP1 cells were infected with vector or Flag-TRIM21 and cultured under GD conditions for 16 h. HA-IPs were analyzed for K48-ubiquitin and HA-IRF4. Inputs are shown as controls. (F) Immunoblot analysis of IRF4 and TRIM21 protein levels in various myeloma cell lines. (G) Correlation analysis of TRIM21 and IRF4 protein levels across myeloma cells from (F). (H) Co-IP of HA-IRF4 with endogenous TRIM21 in ARP1 cells cultured under normal glucose or GD conditions for 16 h. Immunoblotting was detected with antibodies against HA or TRIM21. (I) Co-IP of HA-IRF4 with endogenous TRIM21 in ARP1 cells treated with 2 μM 17-AAG or 120 μM A-769662 for 16 h. (J) HA-IP of HEK293T cells co-expressing HA-IRF4, Strep-TRIM21, and gradient concentrations of Flag-HSP90 to evaluate TRIM21-IRF4 interaction. (K) Domain structure of IRF4 truncation mutants. DBD, DNA-binding domain; LKD, linker domain; IAD, IRF association domain; AR, Association Region. (L-M) Co-IP of IRF4 mutants with Flag-HSP90 (L) or Strep-TRIM21 (M) in HEK293T cells under GD conditions. (N) Proposed model: Metabolic stress activates AMPK, which leads to the nuclear export of HSP90 and compromises the HSP90-IRF4 protein interaction. Data shown as mean ± SD were representative of three independent experiments. **P < 0.01; ***P < 0.001. P values were determined by two-way ANOVA with Bonferroni's post hoc test (C). See also Figure S5.

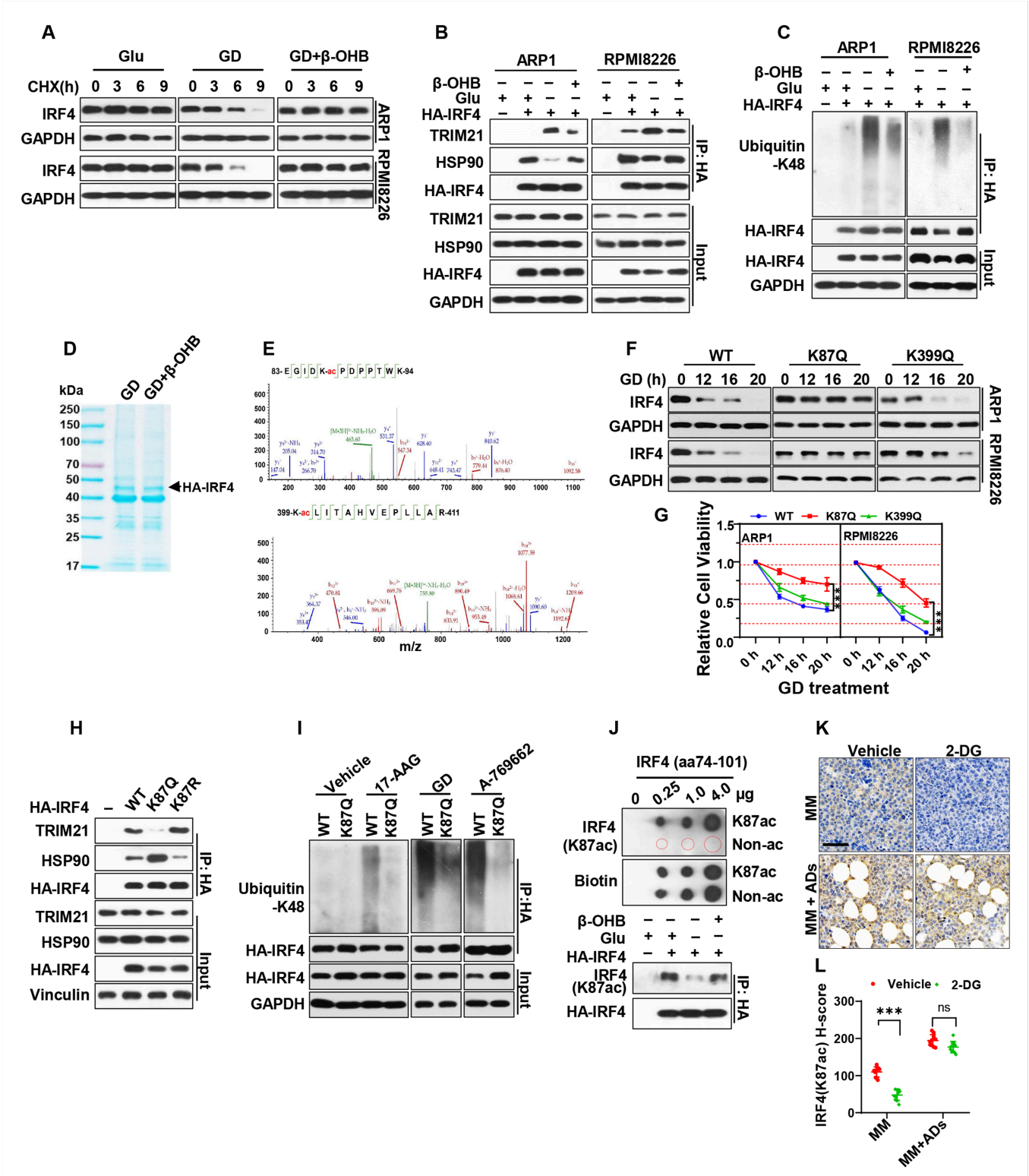


Figure 6

β-OHB triggers IRF4 acetylation to maintain protein stability under GD conditions.

(A) IRF4 protein kinetics in myeloma cells treated with or without 2 mM β-OHB in the presence of CHX under normal glucose or GD conditions. (B) Co-IP of HA-IRF4 with endogenous TRIM21 and HSP90 in myeloma cells treated with or without 2 mM β-OHB under GD conditions. Blots were probed for HA,

TRIM21, or HSP90. (C) IP of HA-IRF4 and immunoblotting for K48-ubiquitin and HA-IRF4 in myeloma cells treated with or without 2 mM β-OHB under normal glucose or GD conditions for 16 h. (D) Coomassie staining of HA-IP eluates (SDS-PAGE) from HA-IRF4-expressing ARP1 cells treated with or without 2 mM β-OHB under GD conditions for 16 h. (E) Mass spectrometry of acetylated lysine at positions 87 and 399 from the cutout HA-IRF4 protein band. (F-G) Protein kinetics of IRF4 (F) and cell viability (G) in myeloma cells expressing either wild-type (WT) HA-IRF4 or acetylation-mimicking mutants (K87Q, K399Q) under GD treatment. (H) Co-IP of HA-IRF4 with endogenous TRIM21 and HSP90 in ARP1 cells expressing WT, K87Q, or acetylation-defective (K87R) HA-IRF4 under GD treatment. (I) IP of HA-IRF4 and immunoblotting for K48-ubiquitin and HA-IRF4 in myeloma cells expressing WT and K87Q HA-IRF4, treated with 2 μM 17-AAG, GD, or 120 μM A-769662 for 16 h. (J) (Upper panel) Specificity validation of custom anti-IRF4-K87ac antibody by dot blot using biotinylated peptides. (Lower panel) HA-IP of lysates from ARP1 cells expressing HA-IRF4 treated with or without β-OHB for 16 h under GD conditions, followed by immunoblotting for IRF4-K87ac. (K) IHC analysis of IRF4-K87ac levels in tumor tissues (from Figure 1I). Scale bar: 100 μm. (L) Quantification of IRF4-K87ac staining intensity using H-scoring. Data shown as mean ± SD were representative of three independent experiments. Ns, non-significant; ***P < 0.001. P values were determined by two-tailed Student’s t-test (L) or two-way ANOVA with Bonferroni's post hoc test (G). See also Figure S6.

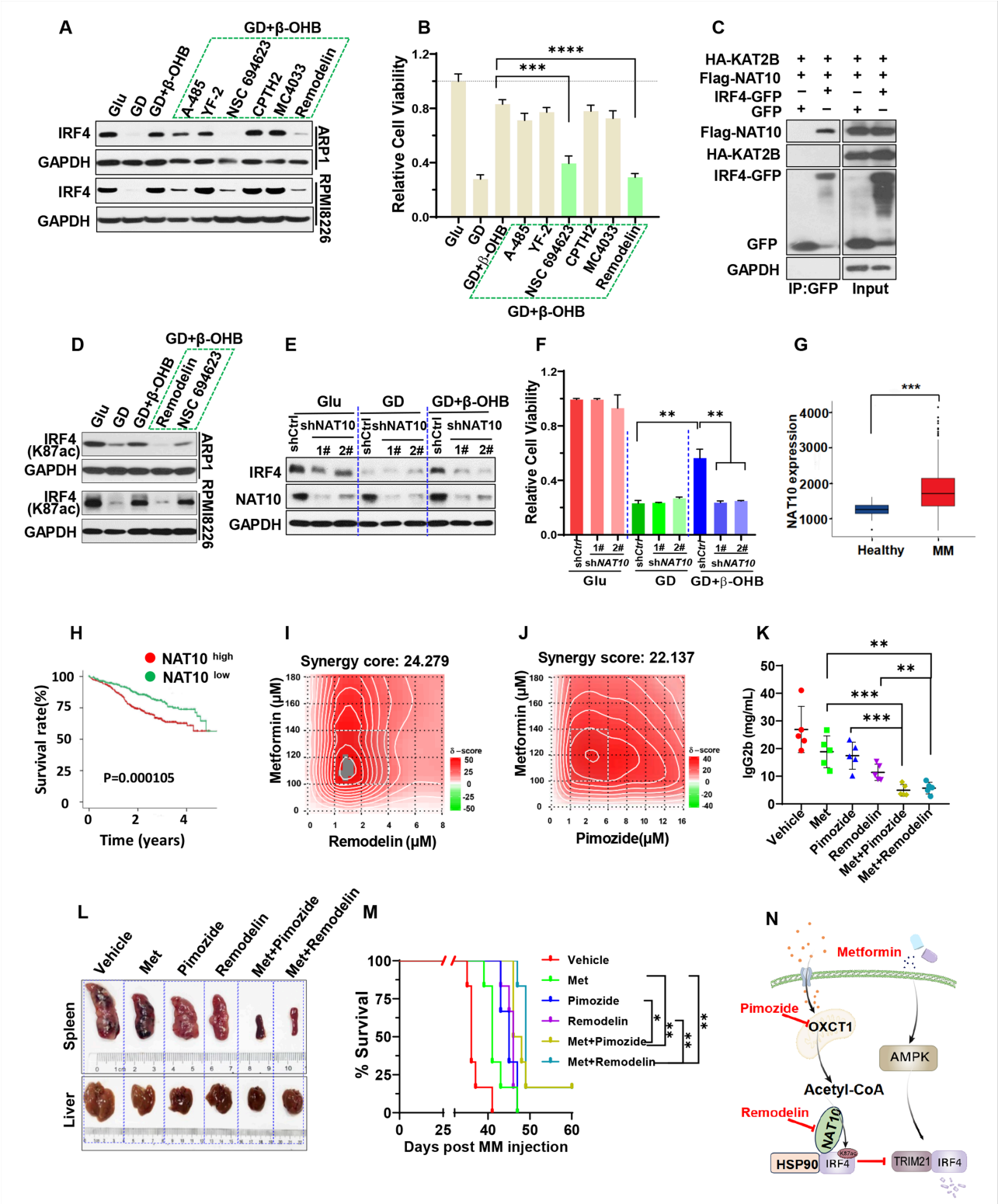


Figure 7

NAT10-mediated IRF4 acetylation promotes myeloma cell survival and represents a therapeutic target

(A-B) IRF4 protein levels (A) and cell viability (B) in myeloma cells treated with 2 mM β-OHB plus 10 μM of various compounds (A-485, YF-2, NSC 694623, CPTH2, MC4033, Remodelin) under GD conditions for 16 h. (C) GFP immunoprecipitation (GFP-IP) in HEK293T cells co-expressing GFP or IRF4-GFP with Flag-

NAT10 and HA-KAT2B, assessing interactions between IRF4 and NAT10 or KAT2B. (D) IRF4 K87ac levels in myeloma cells treated with 2 mM β-OHB plus either 10 μM NSC 694623 or Remodelin under GD conditions for 16 h. (E-F) IRF4 protein levels (E) and cell viability (F) in myeloma cellsexpressing sh*Ctrl*, sh*NAT10*#1, or sh*NAT10*#2, treated with or without β-OHB under normal glucose or GD conditions. (G) *NAT10* mRNA levels in plasma cells from myeloma patients (n=559) versus healthy donors (n=22). (H) Kaplan-Meier survival analysis of myeloma patients stratified by *NAT10*expression (high, n=429; low, n=430) from GEO datasets (GSE2658, GSE5900). P-value by Gehan-Breslow-Wilcoxon test. (I-J) Bliss synergy plots for drug combinations (Metformin plus Remodelin or Pimozide) in ARP1 cells. Analyses performed using SynergyFinder 3.0. (K-M) *In vivo* therapeutic efficacy in Vk12598-transplanted C57BL/6J mice receiving monotherapies (200 mg/kg metformin, 10 mg/kg Remodelin, or 10 mg/kg Pimozide oral) or combination therapies (Metformin+Remodelin or Metformin+pimozide) every other day for 3 weeks. (K) Serum IgG2b levels. (L) Representative spleen/liver images. (M) Kaplan-Meier analysis of mouse overall survival. (N) Proposed model: Synergistic therapeutic strategy combining AMPK activation with NAT10/OXCT1 inhibition in myeloma. Data shown as mean ± SD were representative of three independent experiments. *P < 0.05; **P < 0.01; ***P < 0.001; ****P< 0.0001. P values were determined by a two-tailed Student's t-test (F, K and M). See also Figure S7-S9.

Supplementary Files

This is a list of supplementary files associated with this preprint. Click to download.

- 2.Supplementalinformation.docx